Discrete Wavelet Transform Based Artificial Neural Networks for Extracting Temperature Distributions in Brillouin Optical Time Domain Analysis Sensors

Abul Kalam Azad

Department of Electrical and Electronic Engineering, University of Dhaka, Dhaka-1000, Bangladesh

E-mail: azad@du.ac.bd

ABSTRACT

The uncertainty in extracting temperature distributions using Brillouin optical time domain analysis (BOTDA) sensors depends ultimately on the signal-to-noise ratio (SNR) of the BOTDA-measured Brillouin gain spectra (BGSs) along the fiber. The real-world applications of BOTDA sensors also require fast extraction of temperature distributions from the measured BGSs. To improve the SNR of the measured BGSs, 2D discrete wavelet transform (DWT) based wavelet denoising of BGSs (WDB) is used in this study. The denoised BGSs are then processed by using WDB-based artificial neural networks (WNNs) for the fast and accurate extraction of temperature distributions along a 38.2 km long fiber. The performances of WNNs are investigated in detail for the BGSs acquired from BOTDA experiment at ten different frequency steps and ten different numbers of trace averaging. The effect of WDB as well as WNN on the spatial resolution of the sensors is also analyzed. Moreover, the performances of using WNNs in extracting temperature distributions are compared with that of widely-used nonlinear least-squares fitting (NLF). The experimental results manifest that WNNs can offer much better uncertainty and significantly faster temperature extraction without sacrificing the spatial resolution as compared to NLF. Thus, the proposed WNNs can be effective tools for the fast and accurate extraction of temperature distributions in BOTDA sensors.

1. Introduction

Distributed temperature monitoring over a conventional optical fiber by using Brillouin optical time domain analysis (BOTDA) sensors have attained substantial research interest in recent decades [1-4]. The use of BOTDA sensors enables the precise monitoring of temperature distributions with high spatial resolution [3-5]. In conventional BOTDA sensors, pump and probe waves are initiated at two opposite ends of an optical fiber. These two counter-propagating waves interact within the fiber medium and power supplied by the pump wave amplifies the probe wave. Such amplification process along the fiber is signalized as local Brillouin gain spectrum (BGS). In a local BGS, peak gain arises whenever the pump-probe frequency offset becomes identical to the local Brillouin frequency shift (BFS) of the fiber [1, 6]. As a result, the BOTDA traces collected along the fiber by gradually scanning the pump-probe frequency offsets adjacent to the local BFSs are used to construct the BGSs along the fiber [2, 4]. In reality, thousands of traces are obtained at a specified pump-probe frequency offset which are then averaged to collect one particular trace at that frequency offset so as to improve the trace-SNR to a desired level [6, 7]. The most notable feature of BOTDA sensors is that the BFSs of the BGSs along the fiber vary linearly with local temperatures [2, 3].

The BGS acquired from BOTDA experiment is ideally modelled by Lorentzian profile and nonlinear least-squares fitting (NLS) is usually employed to resolve the BFSs of the BGSs [8, 9]. Then, the linear BFS-temperature characteristics of the fiber are utilized for extracting the temperature distribution from the BFSs along the fiber [2, 8]. However, the uncertainty in extracting temperature distributions using BOTDA sensors is eventually subject to the experimental conditions and depends basically on the frequency step (v_s) used to scan the pump-probe frequency offsets and number of trace averaging (T_a) adopted to collect each BOTDA trace [6, 8]. To reduce the uncertainty, smaller v_s and higher T_a need to be adopted in BOTDA experiment both of which increases the acquisition time of BGSs significantly, especially for a several kilometres long fiber. Moreover, the NLF requires iterative optimization process and thus takes relatively longer runtime [2] for extracting temperature distributions from the BGSs acquired from BOTDA experiment.

In recent years, many techniques alternative to the adaptation of high number of trace averaging have been studied to improve the SNR of the BOTDA-measured BGSs. Such techniques can be broadly classified into two major categories. The techniques belonging to the first category integrate several techniques, such as optical pulse coding [10-12] and distributed Raman amplification [5, 13] with the conventional BOTDA sensor. Consequently, the experimental setup of such sensors becomes complex and expensive. In the techniques belonging to the other category, the noisy measured BGSs obtained from BOTDA experiment adopting lower T_a (i.e., lower SNR) are denoised effectively by using various signal denoising algorithms, such as wavelet transform [14-16], non-local means [16, 17] and anisotropic diffusion [18].

The real-world applications of BOTDA sensors include remote monitoring of fire occurrences in long tunnels, underground mines and large civil structures. Such applications require fast and accurate extraction of temperature distributions along the fiber. For using iterative optimization process, the BGSs processing time of NLF is quite long. The integration of WDB prior to NLF also

includes extra time in the BGSs processing. Consequently, the use of WNNs is proposed and demonstrated in this study to reduce the uncertainty as well as the BGSs processing time of BOTDA sensors. The performances of the proposed WNNs in extracting temperature distributions from the BOTDA-measured BGSs over a 38.2 km long fiber adopting ten different frequency steps as well as ten different numbers of trace averaging are also analyzed in detail.

2. Methods

2.1 BOTDA Setup and the Acquisition of BGSs

The BOTDA setup utilized for the acquisition of BGSs along the fiber is shown in Fig. 1. The laser used in the setup is tuned at 1550 nm to deliver continuous-wave (CW) light in the lower and upper branches via the coupler. The states of polarization of light waves through these branches are maintained by two polarization controllers PC1 and PC2.
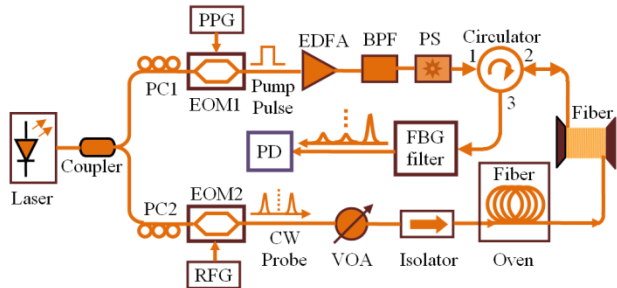

Fig. 1. BOTDA experimental setup for the acquisition of BGSs.

The pump-pulses in the upper branch are generated by modulating the CW light with the help of an electro-optic modulator (EOM1) which is driven by a pulse pattern generator (PPG). The peak pump power is boosted up by using the erbium-doped fiber amplifier (EDFA). The amplified spontaneous emission (ASE) noise is then filtered out by using the band pass filter (BPF). After the states of polarization being randomized by a polarization scrambler (PS) in the upper branch, the pump-pulses finally enter through the near end of the fiber.

The double-sideband suppressed-carrier (DSB-SC) probe wave in the lower branch is generated by modulating the CW light via an additional electro-optic modulator (EOM2) which is driven by a radio frequency generator (RFG). The power of the probe wave is adjusted by means of a variable optical attenuator (VOA). Finally, the isolator in the lower branch allows the propagation of probe signal through the far end of the fiber but stop the propagation of signal from the opposite direction. In this experimental setup, the power from the pump-pulses is transferred to the oppositely directed probe signal. Consequently, the DSB-SC probe wave gets amplified. Finally, the fiber Bragg grating (FBG) filter blocks the undesired upper-sideband of DSB-SC probe wave and the lower-sideband is detected by the photodetector (PD).

The output signal from the PD is scanned step-by-step at a given frequency step (v_s) and time-domain traces along the fiber are obtained by adopting a given number of trace averaging (T_a). The width of the pump-pulses during the BOTDA experiment is set to be 20 ns which ensures 2 m spatial resolution of the sensor. In this demonstration, the last ~0.6 km segment of the 38.2 km long fiber is heated inside a constant-temperature oven keeping the other part outside at room temperature. The distributions of BGSs are obtained along the whole span of the fiber at a sampling rate of 250 Mega-baud that corresponds to 0.4 m along the fiber. The oven temperature is varied from 30 ℃ to 70 ℃ with a step of 10 ℃. The number of trace averaging (T_a) adopted is varied from $T_a = 100$ to 1000 at a step of 100. The BGSs are obtained for a frequency range from 10.76 GHz to 11.01 GHz with a frequency step of $v_s = 1$ MHz. The measured BGSs obtained using $v_s = 1$ MHz at five different temperatures and ten different T_a are under-sampled to get BGSs at nine other larger frequency steps of $v_s = 2$ MHz to 10 MHz at a step of 1 MHz.

2.2 Operating Principle

2.2.1 Wavelet Denoising of BGSs (WDB) Using 2D DWT

In recent years, wavelet transform based signal denoising techniques have attracted great attention due to its distinct capability of multi-resolution analysis and time-frequency representation of signals and images [19 - 22]. In DWT, the scaling function and the corresponding wavelet function are given [14] respectively by

$$\phi_{j,k}(t) = 2^{j/2}\phi(2^j t - k) \tag{1}$$

$$\psi_{j,k}(t) = 2^{j/2}\psi(2^j t - k) \tag{2}$$

where, j and k in Eq. (1) and Eq. (2) are responsible for the scaling and shifting of the functions. In 2D DWT, one 2D scaling function and three 2D wavelet functions are involved. Each of these 2D functions are formed by using 1D scaling function ϕ and corresponding wavelet function ψ as given respectively [20, 23] by

$$\phi_A(p,q) = \phi(p)\phi(q) \tag{3}$$

$$\psi_H(p,q) = \phi(p)\psi(q) \tag{4}$$

$$\psi_V(p,q) = \psi(p)\phi(q) \tag{5}$$

$$\psi_D(p,q) = \psi(p)\psi(q) \tag{6}$$

where p and q are the coordinates of any 2D function $A_0(p, q)$ and ϕ_A, ψ_H, ψ_V and ψ_D are associated with the approximation (A), horizontal detail (HD), vertical detail (VD) and diagonal detail (DD) respectively. The wavelet coefficients of A, HD, VD and DD at level d are now obtained simply by performing the inner products as given [23] respectively by

$$A_{d+1}(m,n) = \langle A_d(p,q), \phi_A(p-2m, q-2n) \rangle \tag{7}$$

$$HD_{d+1}(m,n) = \langle A_d(p,q), \psi_H(p-2m, q-2n) \rangle \tag{8}$$

$$VD_{d+1}(m,n) = \langle A_d(p,q), \psi_V(p-2m, q-2n) \rangle \tag{9}$$

$$DD_{d+1}(m,n) = \langle A_d(p,q), \psi_D(p-2m, q-2n) \rangle \tag{10}$$

In Eq. (7) – Eq. (10), A_d are the approximation coefficients obtained in dth level and for $d = 0$, A_0 is the 2D input

function. It is noteworthy that 2D DWT can be efficiently implemented using filter bank structures incorporating low-pass and high-pass filers [20, 24]. In such implementation, 1D DWT is successively employed to each row and then to each column of the 2D function.

In this work, the noisy measured BGSs acquired along the fiber by utilizing the BOTDA sensor shown in Fig. 1 is used as the 2D function A_0, on which the wavelet denoising of BGSs (WDB) using 2D DWT is performed. Such WDB consists of three sequential steps, i.e., forward-DWT, level-dependent thresholding and inverse-DWT. In forward-DWT, the decomposition filter bank shown in Fig. 2(a) is used to decompose A_0. In the first level decomposition (i.e., $d = 1$) of A_0, four sub bands are obtained comprising wavelet coefficients of approximation (A_1), horizontal detail (HD_1), vertical detail (VD_1) and diagonal detail (DD_1). For decomposing A_0 at a higher level (e.g., $d > 1$), only the approximation coefficients (A_d) obtained from dth level is repetitively decomposed into another four new sub bands as shown in Fig. 2(a) to obtain multi-resolution analysis of BGSs. It is notable that the larger coefficients in the approximation sub band typically contain main features of the BGSs but the smaller coefficients in each of the detail sub bands mostly contain noise features [15, 20].
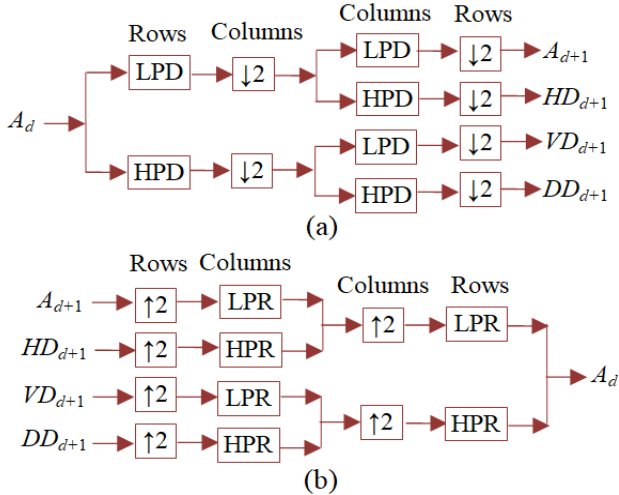

Fig. 2. Filter bank realization of 2D DWT for the (a) decomposition and (b) reconstruction of BGSs using low pass decomposition (LPD) filter, high pass decomposition (HPD) filter, low pass reconstruction (LPR) filter, high pass reconstruction (HPR) filter, down-sampler (↓) and up-sampler (↑).

Next, level-dependent thresholds for all of the detail sub bands are first computed based on Birgé-Massart strategy [20, 25] and then soft thresholding [22] is accomplished only on the detail coefficients keeping the approximation coefficients unchanged. Finally, inverse-DWT is performed on the unchanged approximation sub band and thresholded detail sub bands via the reconstruction filter bank shown in Fig. 2(b) to reconstruct the denoised BGSs. To decompose and reconstruct the BGSs, '*symlet*12' mother wavelet function is used. The coefficients of the decomposition and reconstruction filters used in the implementation of filter banks in Fig. 2 are shown in Fig. 3.
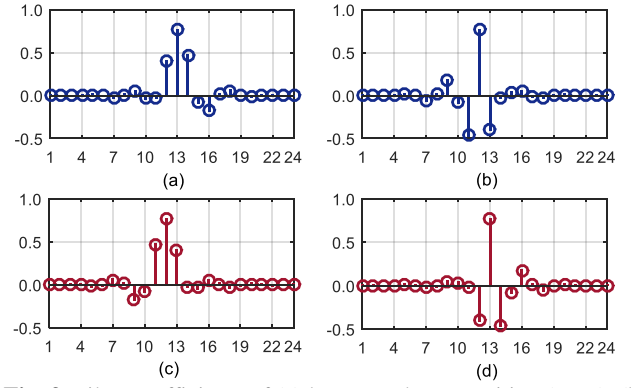

Fig. 3. Filter coefficients of (a) low pass decomposition (LPD), (b) high pass decomposition (HPD), (c) low pass reconstruction (LPR), and (d) high pass reconstruction (HPR) filters.

A visual illustration of level 2 decomposition (i.e., $d = 2$) of typical noisy measured BGSs into different sub bands are shown in Fig. 4. As shown in Fig. 4, the noisy BGSs are first decomposed with $d = 1$ to obtain one approximation sub band (A_1) and three detail sub bands, such as horizontal (HD_1), vertical (VD_1) and diagonal (DD_1). For $d = 2$, A_1 obtained with $d = 1$ is decomposed again which gives another four new sub bands, i.e., A_2, HD_2, VD_2 and DD_2 .
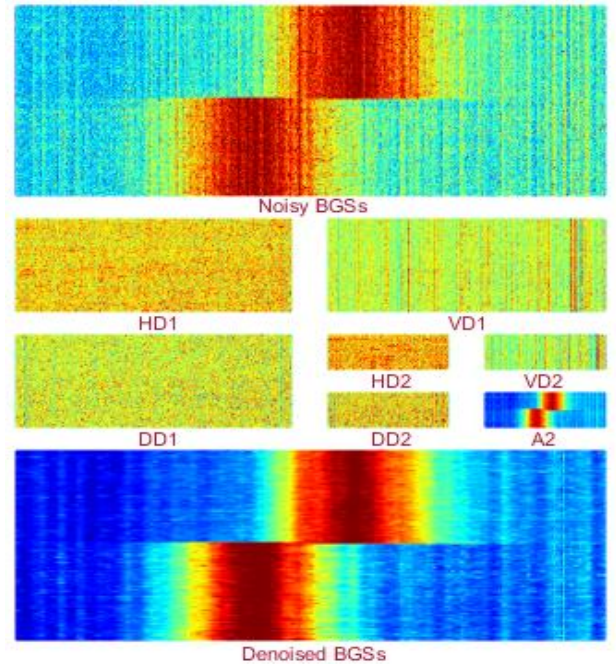

Fig. 4. The diagram depicting the noisy BGSs, decomposed noisy BGSs and reconstructed denoised BGSs with level 2 decomposition in WDB.

The wavelet coefficients in all of the six detail sub bands in Fig. 4 are then soft thresholded but that in A_2 remain unchanged. Finally, the denoised BGSs in Fig. 4 are reconstructed by applying inverse-DWT to the unchanged approximation coefficients and thresholded detail coefficients.

2.2.2 WDB Based Artificial Neural Networks (WNNs)

An ANN is a simplified connectionist system that is widely used for modeling highly nonlinear mapping problems [26 -

29]. Once it is trained with known input-output pairs, it can effectively approximate the outputs for unknown set of inputs. In this study, the extraction of temperature distributions from the BOTDA-measured noisy BGSs employing WNN involves two stages. The noisy BGSs are first denoised by using WDB and then ANN is utilized for extracting temperature distributions from such denoised BGSs. To perform this, ten WNNs are trained separately each suitable to extract temperature distributions from the BGSs acquired at ten different frequency steps of $v_s = 1$ MHz to 10 MHz. To train the WNNs, the known BGS-Temperature (BGS-T) pairs are simulated in view of the BFS-temperature characteristics (i.e., slope of ~0.97497 MHz/°C and intercept of ~10.83415 GHz) of the used fiber [2] and experimental conditions (e.g., pump-pulse width and number of trace averaging, T_a) adopted in BOTDA experiment shown in Fig. 1. In theory, the BGSs acquired from BOTDA experiment are ideally replicated by Lorentzian profile [9, 27]. Thus, the training BGSs in BGS-T pairs are also simulated with Lorentzian profile defined by

$$g(v) = \frac{g_B}{1 + 4\left[(v - v_B)/(\Delta v_B)\right]^2} \tag{11}$$

where, g_B, v_B and Δv_B are the peak Brillouin gain, BFS and line width of each BGS, respectively. In the simulation of training BGSs using Eq. (11), the peak gain of each BGS is set to $g_B = 1$ and the frequency range is fixed from $v = 10.76$ GHz to $v = 11.01$ GHz which is the same as used in the acquisition of BGSs from the BOTDA experiment.

The WNNs are trained in this study to make them suitable for providing temperature output within the range from 0 °C to 100 °C. At a step of 1 °C within this range, the BFS-temperature characteristics of the fiber give the BFSs of a total of 101 BGSs in the range from 10.83415 GHz to 10.93165 GHz with a step of 0.97497 MHz. For adopting 20 ns pump-pulses in BOTDA experimental setup, the line widths of measured BGSs are found to be varied within 50 MHz to 60 MHz due to several factors [2, 8]. To minimize the effect of this variation on the performance of WNNs, the line widths of each of the 101 BGSs are also varied within 50 MHz to 60 MHz at 1 MHz step by keeping their BFSs unchanged. Consequently, a total of 101×11 ideal BGSs are simulated by using Eq. (11) to accommodate the required temperature and line width ranges. The measured BGSs acquired from BOTDA-experimental setup are noisy and the noise level of the BGSs varies with distance along the fiber. This level of noise also depends on the number of trace averaging (T_a) used in BOTDA experiment [6, 7]. For the proper matching of the training BGSs with the noisy measured BGSs, the simulated clean BGSs are contaminated by adding adaptive-white-Gaussian-noise (AWGN) with varying SNR ranging from 12 dB to 25 dB at a step of 1 dB. Finally, a total of $(101 \times 11 \times 14)$ 15554 BGS-T pairs are simulated for training the WNNs. Within the frequency range from $v = 10.76$ GHz to $v = 11.01$ GHz, the noisy training BGSs suitable to train ten WNNs are simulated by adopting ten different frequency steps (v_s). It is worth to mention that the mapping capability of WNNs is subject to the similarities between the BGSs used in training and testing phases. Since the measured BGSs are denoised by applying WDB before being fed to the trained WNNs for extracting temperature distributions in the testing phase, the noisy training BGSs obtained at each of the ten v_s are also denoised by using WDB. The denoised training BGSs are then normalized within the range from 0 to 1 [27, 28]. Finally, each set of BGS-T pairs simulated at a particular v_s is used to train each of the ten WNNs to make them suitable for extracting temperature distributions from the BGSs acquired at that v_s.

The pyramid-shaped architecture of each of the ten WNNs consists of two hidden layers as shown in Fig. 5. The number of neurons in the input layer of each WNN in Fig. 5 at a particular v_s is that of sample points on the BGSs at that v_s. To provide temperature output, there is only one neuron in the output layer of each WNN. For simplicity, the first and second hidden layers of each WNN contain approximately half and one-quarter of neurons used in the input layer respectively. Each of the ten different WNNs at ten different v_s is trained separately using corresponding BGS-T pairs via back propagation algorithm [27 - 29]. Once the training processes of WNNs are accomplished, each of the ten trained and optimized WNNs is utilized directly to extract temperature distributions from the denoised BGSs attained at each of the ten different frequency steps.
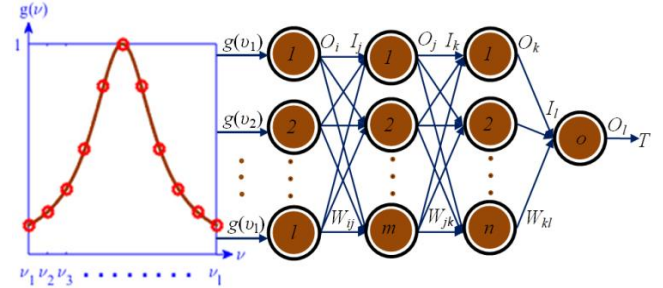

Fig. 5. A typical two-hidden-layer WNN used to extract temperature distributions from the denoised BGSs.

2.2.3 Nonlinear Least-Squares Fitting (NLF)

To compare the performance of WNN with that of NLF, the distributions of temperature from the BOTDA-measured BGSs along the fiber are also determined using NLF. For this, each measured BGS along the fiber is fitted individually by the Lorentzian profile defined in Eq. (11) and the BFS of such BGS is supposed to be equal to the fitted v_B. The BFS distributions along the fiber are then transformed to temperature distributions utilizing the linear BFS-temperature characteristics of the fiber. A detailed description of the NLF is available in Ref. [14, 27].

3. Results and Discussion

3.1 Performance Analysis of WDB

In this study, the BGSs along the full length of a 38.2 km fiber are obtained by heating its last ~0.6 km segment with a constant-temperature oven each time at 30 °C, 40 °C, 50 °C, 60 °C and 70 °C. For this five oven temperatures, the

BGSs are obtained using frequency steps of $v_s = 1$ MHz to $v_s = 10$ MHz at 1 MHz step with varying T_a starting from $T_a = 100$ and ending to $T_a = 1000$ with an increment of 100. As an example, the distribution of BOTDA-measured BGSs obtained along the 38.2 km long fiber for oven temperature of 70 °C at $v_s = 1$ MHz and $T_a = 500$ is shown in Fig. 6.
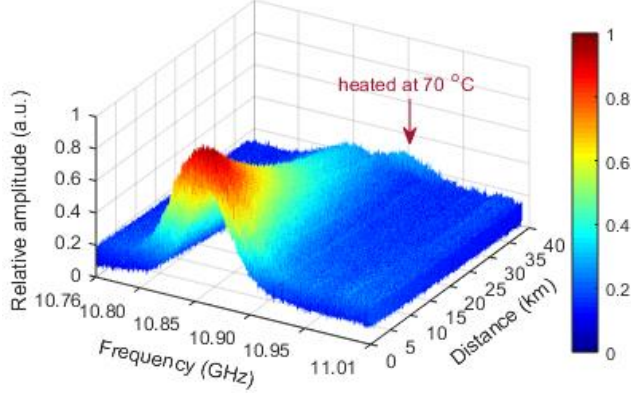

Fig. 6. Distribution of measured BGSs obtained at $v_s = 1$ MHz and $T_a = 500$ for the last ~0.6 km of the 38.2 km fiber heated at 70 °C.

The measured BGSs acquired from BOTDA experiment with each of these five temperatures, ten v_s and ten T_a are denoised separately by using WDB. In WDB, five different levels (i.e., $d = 1$ to 5) of BGSs decomposition and reconstruction are adopted. The denoised BGSs obtained after applying WDB with $d = 2$ to the measured BGSs in Fig. 6 are shown in Fig. 7.
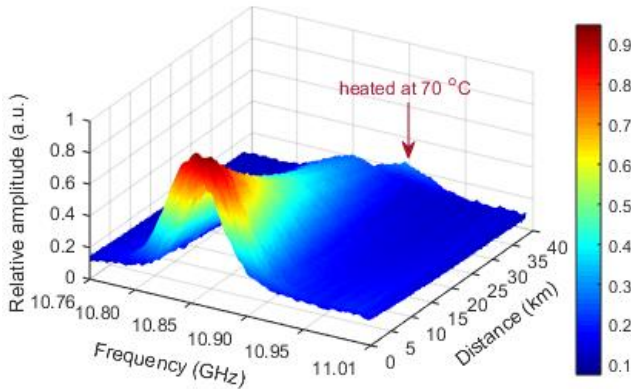

Fig. 7. Distribution of denoised BGSs after applying WDB with $d = 2$ to the measured BGSs obtained at $v_s = 1$ MHz and $T_a = 500$ for the last ~0.6 km of the 38.2 km fiber heated at 70 °C.

It is observed that the noise level of the denoised BGSs shown in Fig. 7 is much lower than that of the measured BGSs shown in Fig. 6. To observe the denoising performance of WDB more clearly, the measured trace at 10.86 GHz in Fig. 6 and the corresponding denoised trace in Fig. 7 are plotted in Fig. 8. It is easy to notice in Fig. 8 that WDB can reduce noise from the measured trace significantly. In fact, the reduction of noise from the measured traces is associated with the reduction of noise from measured BGSs. As a result, WDB also helps to enhance the SNR of the measured BGSs accordingly.
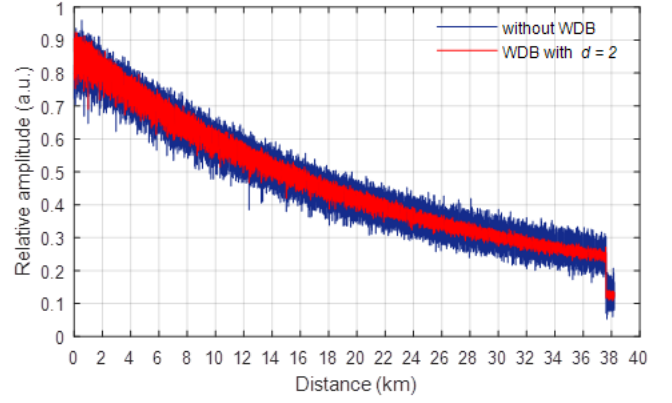

Fig. 8. The measured trace and the corresponding denoised trace after applying WDB with $d = 2$ to the BGSs obtained at $v_s = 1$ MHz and $T_a = 500$ for the last ~0.6 km of the 38.2 km fiber heated at 70 °C.

The results presented in Fig. 7 and Fig. 8 visually illustrate the denoising performance of level 2 (i.e., $d = 2$) WDB. In practice, WDB can be applied with different levels of BGSs decomposition and its performance can be evaluated in term of SNR. For this, the SNRs of the measured and denoised traces along the last 0.5 km segment of the fiber are computed where the SNRs are reasonably lowest. Since the last 0.5 km segment of the fiber is heated each time at one of the five different temperatures, their peak gain frequencies are also different and vary linearly with temperature [2, 27]. Thus, the traces for calculating SNRs at five different temperatures are selected at five different frequencies corresponding to their peak gain frequencies. Then the SNR of each trace at different temperatures is calculated to be the ratio of the average of the trace amplitudes along the last 0.5 km fiber to the standard deviation of such trace amplitudes [16]. At a particular T_a and d, five nearly equal SNRs are computed for five different temperatures which are then averaged to approximate the SNR at that T_a and d. The variation of SNRs of measured traces without applying WDB and that of denoised traces obtained after applying WDB is shown in Fig. 9.
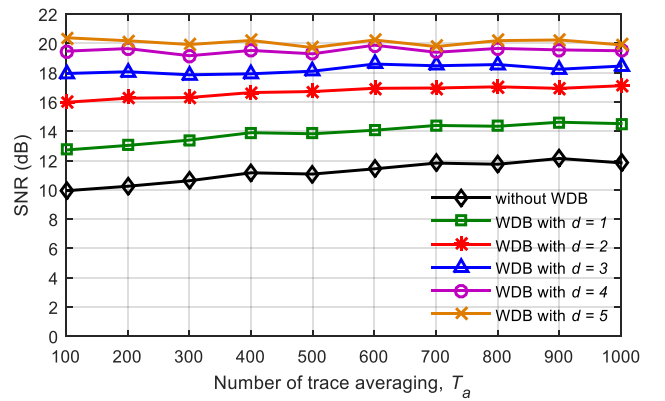

Fig. 9. Variation of SNRs computed along the last 0.5 km segment of the 38.2 km long fiber.

It is seen in Fig. 9 that the SNRs of the measured and denoised traces increase with T_a. This is reasonable because averaging of more traces also helps to improve the trace-

SNR. It is also seen in Fig. 9 that the SNRs of the denoised traces obtained after applying WDB with different d are also higher than that without applying WDB at each of the ten different T_a. For instant, the SNR for the measured trace (i.e., without WDB) at $T_a = 500$ is 11.08 dB which improves gradually by 2.75 dB, 5.63 dB, 7.02 dB, 8.21 dB and 8.63 dB for applying WDB with $d = 1$, 2, 3, 4 and 5 respectively. This means that the use of WDB with higher level of BGSs decomposition also provides higher improvement of SNR.

The results in Fig. 9 indicate that WDB with higher level (i.e., higher d) of BGSs decomposition offers better SNR. However, these higher SNRs are attained by thresholding high frequency components of BGSs in WDB. Therefore, the denoised traces turn to be over-smoothed. This becomes more severe along the fiber segment where drastic transition of traces takes place for sudden change in temperature [14, 24]. As a result, WDB with higher d also deteriorates the spatial resolution of the sensor. To verify this effect, the measured trace at 10.86 GHz along the fiber for adopting maximum oven temperature of 70 °C in this work is considered. The measured trace is denoised by applying WDB with five different levels of BGSs decomposition. The measured and denoised traces along the fiber segment from 37.613 km to 37.619 km where the temperature changes suddenly from room temperature to 70 °C are plotted in Fig. 10.
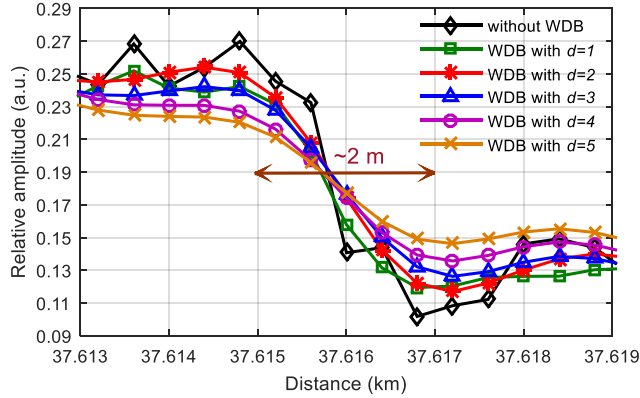

Fig. 10. The measured trace at 10.86 GHz and its denoised traces along the fiber segment where temperature changes suddenly from room temperature to 70 °C.

It is observed in Fig. 10 that the spatial resolution of the sensor degrades gradually if WDB with higher d is used. The results in Fig. 10 also confirm that the traces denoised by applying WDB with $d = 1$ and 2 can conserve the spatial resolution of the sensor which is 2 m in this demonstration. However, it is also necessary to sacrifice the spatial resolution of the sensor if WDB with $d > 2$ is applied.

3.2 Performance Analysis of WNNs

For extracting temperature distributions by employing WNNs, ten WNNs are trained separately. The measured BGSs are first denoised by using WDB with $d = 2$ and these denoised BGSs are then normalized within the range from 0 to 1. Such BGSs are finally supplied to the trained WNNs for directly extracting the temperature distributions. It is worth to mention that each of the ten WNNs trained for a

particular v_s involves in the temperature distribution extraction from the BGSs acquired at that v_s adopting all of the ten different T_a and five different oven temperatures. For instance, the distributions of temperature along the 38.2 km long fiber extracted by WNN trained for $v_s = 1$ MHz from the measured BGSs obtained at $v_s = 1$ MHz and $T_a = 1000$ with the last ~0.6 km fiber segment heated at five different oven temperatures are shown in Fig. 11. For comparison, the distributions of temperature extracted by NLF from the measured BGSs obtained under same experimental conditions are also shown in Fig. 12.
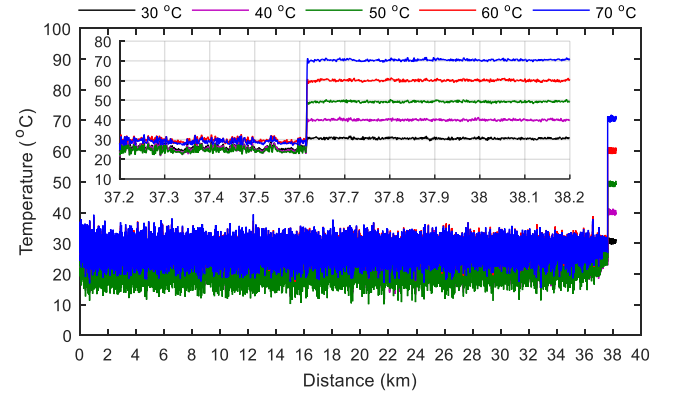

Fig. 11. WNN extracted temperature distributions from the measured BGSs along the 38.2 km fiber acquired at $v_s = 1$ MHz, $T_a = 1000$ with the last ~0.6 km fiber segment heated at five different temperatures. Inset: temperature distributions along the last 1 km fiber segment.

Fig. 12. NLF extracted temperature distributions from the measured BGSs along the 38.2 km fiber acquired at $v_s = 1$ MHz, $T_a = 1000$ with the last ~0.6 km fiber segment heated at five different temperatures. Inset: temperature distributions along the last 1 km fiber segment.
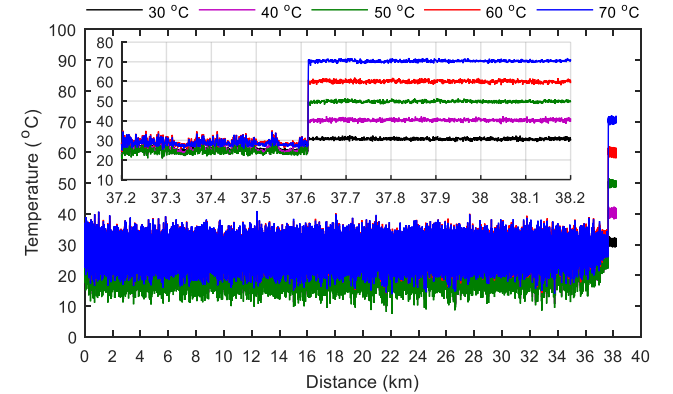
It is easily seen in Fig. 11 that WNN is able to extract temperature distributions along the 38.2 km long fiber satisfactorily. The temperature distributions extracted by WNN in Fig. 11 also exhibit much reduced fluctuation (i.e., lower uncertainty) as compared to that extracted by NLF in Fig. 12. It is also seen in Fig. 11 that WNN extracted temperature distributions along the last ~0.6 km fiber segment heated at five different oven temperatures are very consistent. It is noteworthy that the room temperature external to the oven during the experiment is not maintained exactly at a constant level. As a result, the temperature

distributions along the fiber segment that remains external to the oven also fluctuate slightly over time.

In this study, the effect of levels of BGSs decomposition (d) in WDB on the spatial resolution of the sensor is also verified for using WNN. For comparing the effect with the results shown in Fig. 10, the measured BGSs obtained for 70 °C at $v_s = 1$ MHz and $T_a = 500$ are denoised by using WDB with five different d. The WNN trained for $v_s = 1$ MHz is then used to extract temperature distributions. To observe the effect clearly, the distributions of temperature along the fiber segment from 37.613 km to 37.619 km where the temperature suddenly changes from room temperature to 70 °C are plotted in Fig. 13.
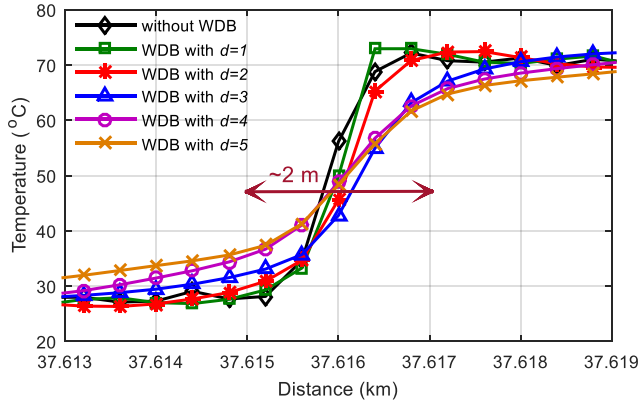

Fig. 13. Temperature distributions along the fiber segment where temperature changes suddenly from room temperature to 70 °C.

Similar to the results observed from denoised traces in Fig. 10, it is also observed from the temperature distributions provided by WNN in Fig. 13 that WDB with maximum decomposition level of $d = 2$ can only preserve the 2 m spatial resolution of the sensor. If WDB is applied with $d > 2$, the spatial resolution of the sensors requires to be sacrificed. Consequently, the performances of WNNs in extracting temperature distributions from the BGSs denoised by using WDB only with $d = 2$ are analyzed next.

The results shown in Fig. 11 and Fig. 12 reveal that the temperature distributions extracted by WNN at all of the five different oven temperatures provide much lower uncertainties as compared to that extracted by NLF for the BGSs obtained using $v_s = 1$ MHz, $T_a = 1000$. To compare the uncertainties provided by WNN and NLF at each v_s and T_a, the last 0.5 km from 37.7 km to 38.2 km fiber segment heated inside the oven is considered. The uncertainty provided by WNN or NLF is then computed to be the standard deviation of temperatures [2, 6] along this fiber segment extracted by WNN or NLF respectively. At a particular v_s and T_a, WNN provides five nearly-equal uncertainties for each of the five different temperatures. These nearly-equal uncertainties are then averaged to estimate the uncertainty provided by WNN at that v_s and T_a. Similarly, the uncertainty provided by NLF is also obtained at a particular v_s and T_a. The uncertainties offered by WNN and NLF for all v_s and T_a are plotted in Fig. 14.
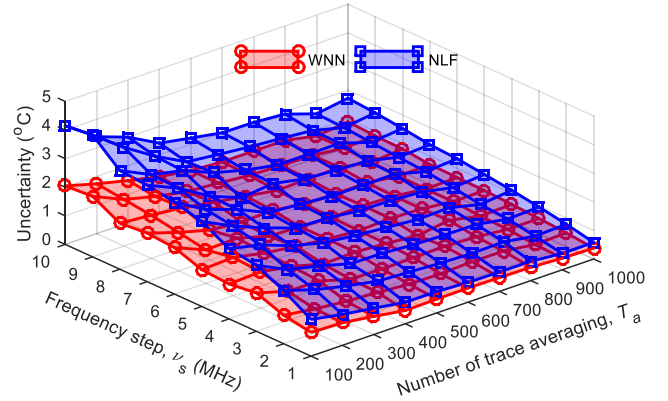

Fig. 14. Uncertainties in extracting temperature distributions.

It is noticed in Fig. 14 that uncertainties provided by both of these two methods increase gradually if BGSs along the fiber are acquired at higher frequency steps (i.e., fewer sample points on BGSs) and lower numbers of trace averaging (i.e., lower SNR). It is also clear in Fig. 14 that the uncertainty provided by WNN at each v_s and T_a is much smaller than that provided by NLF. Thus, WNN can significantly improve the uncertainty of BOTDA sensor in extracting temperature distributions along the fiber. For instances, the uncertainties in Fig. 14 using NLF at $T_a = 100$ for v_s of 1 MHz, 5 MHz and 10 MHz are 1.28 °C, 2.97 °C and 4.15 °C respectively which have been reduced to 0.83 °C, 1.29 °C and 2.05 °C respectively for using WNN. In Fig. 14, NLF and WNN provide lowest uncertainties of 0.58 °C and 0.38 °C respectively at $v_s = 1$ MHz and $T_a = 1000$ in this study. However, WNN provides uncertainties of 0.63 °C at $v_s = 1$ MHz and $T_a = 300$; 0.61 °C at $v_s = 4$ MHz and $T_a = 1000$; and 0.56 °C at $v_s = 2$ MHz and $T_a = 600$ which are comparable to that of 0.58 °C provided by NLF at $v_s = 1$ MHz and $T_a = 1000$. Consequently, the uncertainty provided by NLF at $v_s = 1$ MHz and $T_a = 1000$ is comparable to that offered by WNNs with either ~3.33 times less T_a, ~4 times more v_s or 1.67 time less T_a and ~2 time more v_s. This implies that WNN offers significantly faster acquisition of BGSs along the fiber from BOTDA experiment as compared to NLF but can achieve comparable uncertainty in extracting temperature distributions.
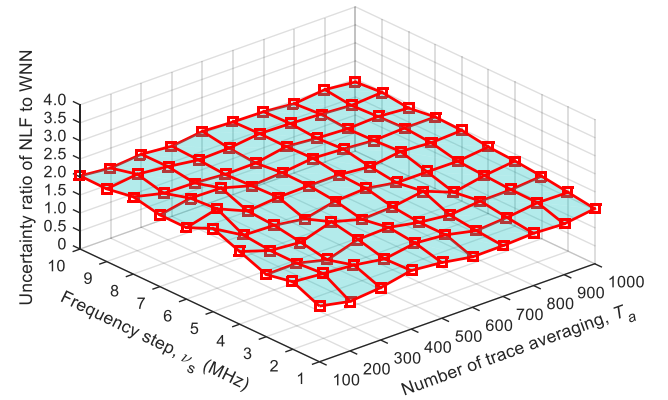

Fig. 15. Variation of uncertainty ratio in extracting temperature distributions for using NLF to that for using WNN.

Next, the performance of WNN is compared with that of NLF in term of ratio of uncertainties. For this, the

uncertainty provided by NLF at each v_s and T_a is divided by that provided by WNN. The results are shown in Fig. 15 where a ratio greater than 1 means lower uncertainty (i.e., better performance) for using WNN compared to that for using NLF.

The results shown in Fig. 15 confirm that the uncertainty given by WNN at each v_s and T_a is ~2 times lower than that given by NLF, especially at higher v_s and lower T_a. For instance, uncertainty ratio of NLF to WNN at $v_s = 10$ MHz and $T_a = 100$ is 2.03, i.e., uncertainty provided by WNN is 2.03 times lower than that provided NLF. However, the uncertainty ratio decreases a little for the BGSs along the fiber obtained at lower v_s and higher T_a as also observed in Fig. 15. For example, uncertainty ratios at $v_s = 5$ MHz are 2.31, 1.86 and 1.85 for T_a of 100, 500 and 1000 respectively while that at $T_a = 500$ are 1.54, 1.86 and 2.06 for v_s of 1 MHz, 5 MHz and 10 MHz respectively. It should be noted that the average uncertainty ratio in Fig. 15 is ~1.84. This implies that uncertainty for using WNN is, on an average, ~1.84 times lower than that for using NLF.

Finally, the runtimes of trained WNN and NLF in extracting distributions of temperature from the BGSs along the fiber are compared and analyzed. For this comparison, the runtimes required by WNN and NLF to extract such distributions from the BGSs acquired at each v_s and T_a for each of the five different temperatures are determined individually. The runtimes of WNN or NLF at each v_s and T_a are then determined to be the average of runtimes required for these five temperatures for using WNN or NLF respectively. It is worth to mention that the runtime determined for WNNs at each v_s and T_a incorporates the runtimes required by WDB to denoise the measured BGSs as well as that required by WNN to extract temperature distributions from the denoised BGSs. To compare the runtimes of WNN and NLF, the runtime ratio of NLF to WNN is computed by dividing the runtimes of NLF with that of WNN at each v_s and T_a. The results are plotted in Fig. 16.
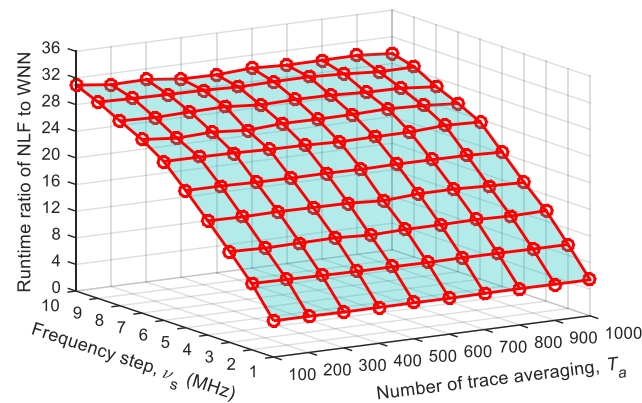

Fig. 16. Variation of runtime ratio in extracting temperature distributions for using NLF to that for using WNN.

The results in Fig, 16 clearly reveal that runtime ratio of NLF to WNN is much larger than 1 (e.g., ranges from ~5.38 to 30.94) at different v_s and T_a. Thus, the extraction of temperature distributions from BGSs along the fiber using

WNN requires much shorter runtimes as compared to NLF. It is also seen in Fig. 16 that the runtime ratio for the BGSs obtained a particular v_s is almost the same and does not vary significantly with T_a. However, the runtime ratio of NLF to WNN increases rapidly if larger v_s is adopted in BOTDA experiment to acquire the BGSs along the fiber. For instances, the runtime ratios in Fig. 16 at $T_a = 500$ are 5.40, 13.67, 23.55 and 29.72 for v_s of 1 MHz, 3 MHz, 6 MHz and 10 MHz, respectively. This implies that temperature distribution extraction along the fiber from the BGSs acquired from BOTDA experiment at frequency steps of 1 MHz, 3 MHz, 6 MHz and 10 MHz are also 5.40, 13.67, 23.55 and 29.72 times faster as compared to NLF. The larger runtime ratio of NLF to WNN is due to the fact that NLF optimizes the model parameters iteratively and thus requires relatively longer runtime [14, 27]. On the other hand, the testing phase of a trained WNN is very straightforward and thus requires relatively shorter runtime [26, 27] as compared to NLF for temperature distribution extraction from the BGSs along the fiber.

4. Conclusions

In this paper, the use of WDB based ANNs (WNNs) is proposed and experimentally demonstrated for the fast and accurate extraction of temperature distributions along a 38.2 km fiber. The training of WNNs with AWGN added BGSs possessing variable linewidths makes the proposed method more pragmatic. The proposed WNNs can be effectively applied to process the BGSs acquired from BOTDA experiment with 20 ns pump-pulses for extracting temperature distributions within the range from 0 ºC to 100 ºC. However, the training process of WNNs with simulated BGSs can easily be customized for other experimental conditions. In this study, the effect of using different levels of BGSs decomposition in WDB is analyzed in detail and level 2 BGSs decomposition is used safely in WNNs to retain the 2 m spatial resolution of the sensor. The performances of WNNs are also compared with that of traditional NLF for the BGSs acquired at ten different frequency steps and ten different numbers of trace averaging. The results signify that the uncertainties in extracting temperature distributions provided by WNNs are almost half as compared to that provided by NLF. Moreover, the extraction of temperature distributions by using WNN is several times faster than that by using NLF. Therefore, the fast and accurate extraction of temperature distributions by using the proposed WNN can be an attractive alternative to make BOTDA sensors more suitable for real-world applications.

References

1. H. Zhang, D. Zhou, B. Wang, C. Pang, P. Xu, T. Jiang, D. Ba, H. Li, and Y. Dong, "Recent Progress in Fast

Distributed Brillouin Optical Fiber Sensing," *Appl. Sci*, vol. 8, no. 10, pp. 1820, 2018.

2. A. K. Azad, F. N. Khan, W. H. Alarashi, N. Guo, A. P. T. Lau, and C. Lu, "Temperature extraction in Brillouin optical time-domain analysis sensors using principal component analysis based pattern recognition," *Opt. Express*, vol. 25, no. 14, pp 16534-16549, 2017.

3. Y. Dong, "High-Performance Distributed Brillouin Optical Fiber Sensing," *Photonic Sensors*, vol. 11, no. 1, pp. 69-90, 2021.

4. S. Wang, Z. Yang, S. Zaslawski, and L. Thévenaz, "Short spatial resolution retrieval from a long pulse Brillouin optical time-domain analysis trace," *Opt. Lett.*, vol. 45, no. 15, pp. 4152-4155, 2020.

5. X. Angulo-Vinuesa, S. Martin-Lopez, P. Corredera, and M. Gonz´alez-Herr´aez, "Raman-assisted Brillouin optical time-domain analysis with sub-meter resolution over 100 km," *Opt. Express*, vol. 20, no. 1), pp. 12147-12154, 2012.

6. M. A. Soto, and L. Thévenaz, "Modeling and evaluating the performance of Brillouin distributed optical fiber sensors," *Opt. Express*, vol. 21, no. 25, pp. 31347-31366, 2013.

7. S. Wang, Z. Yang, M. A. Soto, and L. Thévenaz, "Study on the signal-to-noise ratio of Brillouin optical time-domain analyzers," *Opt. Express*, vol. 28, no. 14, pp. 19864-19876, 2020.

8. A. Motil, A. Bergman, and M. Tur, "State of the art of Brillouin fiber-optic distributed sensing," *Opt. & Laser Technol.*, vol. 78, no. A, pp. 81-103, 2016.

9. S. M. Haneef, Z. Yang, L. Thévenaz, D. Venkitesh, and B. Srinivasan, "Performance analysis of frequency shift estimation techniques in Brillouin distributed fiber sensors," *Opt. Express,* vol. 26, no. 11, pp. 14661-14677, 2018

10. M. A. Soto, G. Bolognini, F. Di Pasquale, and L. Thévenaz, "Long-range optical time-domain analysis employing pulse coding techniques," *Meas. Sci. Technol.* vol. 11, no. 9, pp. 1–7, 2010.

11. H. Iribas, A. Loayssa, F. Sauser, M. Llera, and S. L. Floch, "Cyclic coding for Brillouin Optical Time-Domain Analyzer using probe dithering," *Opt. Express*, vol. 25, no. 8, pp. 8787-8800, 2017.

12. C. Zhao, M. Tang, R. Liao, H. Wu, and S. Fu, "SNR-Enhanced Fast BOTDA Combining Channel Estimation Technique with Complementary Pulse Coding," *IEEE Photonics. J.*, vol. 10, no. 5, pp. 1-10, 2018.

13. X. Jia, and Y. Rao, L. Chang, C. Zhang and Z. Ran, "Enhanced sensing performance in long distance Brillouin optical time-domain analyzer based on Raman amplification: Theoretical and experimental investigation," *J. Lightwave Technol.* vol. 28, no. 11, pp. 1624–1630, 2010.

14. A. K. Azad, "Analysis of 2D Discrete Wavelet Transform Based Signal Denoising Technique in Brillouin Optical Time Domain Analysis Sensors," The Dhaka University JASE, vol. 5, no. 1&2, pp. 1-8, 2020.

15. M. A. Farahani, M. T. V. Wylie, E. Castillo-Guerra, and F. G. Colpitts, "Reduction in the number of averages required in BOTDA sensors using wavelet denoising techniques," *J. Lightwave Technol*. vol. 30, no. 8, pp. 1134–1142, 2012.

16. M. A. Soto, J. A. Ramírez, and L. Thévenaz, "Intensifying the response of distributed optical fibre sensors using 2D and 3D image restoration," *Nat. Commun.* vol. 7, p. 10870, 2016.

17. X. Qian, X. Jia, Z. Wang, B. Zhang, N. Xue, W. Sun, Q. He and H. Wu, "Noise level estimation of BOTDA for optimal non-local means denoising," *Appl. Optics*, vol. 56, no. 16, pp. 4727-4734, 2017.

18. K. Luo, B. Wang, N, Guo, K. Yu, C. Yu, and C. Lu "Enhanced SNR by Anisotropic Diffusion for Brillouin Distributed Optical Fiber Sensors," *J. Lightwave Technol.* vol. 38, no. 20, pp. 5844–5852, 2020.

19. A. Shahbahrami, "Algorithms and architectures for 2D discrete wavelet transform," *J. Supercomput*, vol. 62, pp. 1045-1064, 2012.

20. S. Sidhik, "Comparative study of Birge–Massart strategy and unimodal thresholding for image compression using wavelet transform," *Optik- Int. J. for Light & Elect. Optics*, vol. 126, no. 24, pp. 5952-5955, 2015.

21. M. N. Abdulwahed, and A. K. Ahmed, "Underwater Image De-noising using Discrete Wavelet Transform and Pre-Whitening Filter," *Telkomnika*, vol. 16, no. 6, pp. 2622-2629, 2018.

22. L. Feng, and L. Lin, "Comparative Analysis of Image Denoising Methods based on Wavelet Transform and Threshold Functions," *IJE. Trans. B: Applications*, vol. 30, no. 2, pp. 199-206, 2017.

23. K. M. Iftekharuddin, and A. A. Awaal, Field Guide to Image Processing, Electrical & Computer Engineering Faculty Books, SPIE Press, Bellingham, Washington, pp 67-68 , 2012.

24. A. SOVIĆ, and D. SERŠIĆ, "Signal decomposition methods for reducing drawbacks of DWT," *Eng. Rev*. vol. 32, no. 2, pp. 70–77, 2012.

25. K. Daqrouq, I. N. Abu-Isbeih, O. Daoud, and E. Khalaf, "An investigation of speech enhancement using wavelet filtering method," *Int. J. speech Technol.* vol. 13, no. 2, pp. 101-115, 2010.

26. A. K. Azad, L. Wang, N. Guo, C. Lu, and H. Y. Tam, "Temperature sensing in BOTDA system by using artificial neural network," *Electron. Lett*. vol. 51, no. 20, pp. 1578–1580, 2015.

27. A. K. Azad, L. Wang, N. Guo, H. Y. Tam and C. Lu, "Signal processing using artificial neural network for BOTDA sensor system," *Opt. Express*, vol. 24, no. 6, pp. 6769-6782, 2016.

28. G. Zhang, B. E. Patuwo, and M. Y. Hu "Forecasting with Artificial Neural Networks: The state of the art," *Int. J. forecasting*, vol. 14, no. 1, pp. 35-62, 1998.

29. A. Suliman, and Y. Zhang, "A review on Back-Propagation Neural Networks in the Application of Remote Sensing Image Classification," *J. Earth Sci. & Engg.*, vol. 5, pp. 52-65, 2015.